Supplemental Material for:

Finite-Size Effect in Phonon-Induced Elliott-Yafet Spin Relaxation in Al

J. D. Watts,[1,2] J. T. Batley,[2] N.A. Rabideau,[2] J.P. Hoch,[2] L. O'Brien,[2,3]
P.A. Crowell,[1] and C. Leighton[2]

[1] School of Physics and Astronomy, University of Minnesota,
Minneapolis, Minnesota, 55455, USA

[2] Department of Chemical Engineering and Materials Science, University of Minnesota,
Minneapolis, Minnesota, 55455, USA

[3] Department of Physics, University of Liverpool,
Liverpool L69 3BX, UK

Section A: Fabrication and Measurement Details

As in our prior work [*e.g.*, S1,S2], bilayer resist masks were formed on Si/Si-N substrates in a Vistec EBPG 5000+ system, followed by multi-angle deposition to define Co/Al NLSVs in a single shot. Ultra-high vacuum (UHV, base pressure $O(10^{-10}$ Torr)) electron beam evaporation was employed for metal deposition, using 99.999% purity Al, with both Co and Al deposited at 0.5 Å s^{-1}, at ~5×10^{-9} and ~1×10^{-8} Torr, respectively. Lateral grain sizes in the Al (from atomic force microscopy) varied from approximately 50 nm at low thickness to 150 nm at the highest thickness. Typical final N (Al) channel widths, w_N, were 150 nm; F (Co) injector and detector widths (w_F) were 75 and 50 nm, to achieve distinct coercivities. To accommodate differences between the Al N channel thickness (t_N) and the Co F thickness (t_F), we deposited 16 nm of Co prior to Al for $t_N \geq 25$ nm (*i.e.*, Co first then Al second for thick channels), or 32 nm of Co subsequent to Al for $t_N \leq 25$ nm (*i.e.*, Al first then Co second for thin channels). This avoids issues with very thin Al channels failing to contour the F at low t_N.

Importantly, the above choice with respect to the N/F deposition order does not appreciably influence any of the t_N dependencies probed in this work. This is apparent in Figs. 1(c,d), 2(c), 3(b-d), and 4(c), where no form of discontinuity or anomaly is apparent around $t_N = 25$ nm. Fig. S1 below shows this more explicitly, plotting the spin accumulation signal ΔR_{NL} *vs.* t_N for a typical injector/detector separation $d = 250$ nm, at both low (5 K) and high (275 K) temperature, for NLSVs deposited "Al first" (red triangles) or "Al second" (blue diamonds, grey circles). Note that we show here not only data on the devices on Si/Si-N substrates studied throughout this work, but

also additional data on devices on Al_2O_3 substrates. As can be seen clearly in the figure, no significant discontinuity or anomaly is apparent around t_N = 25 nm. Note here that despite any change in Co resistivity due to the use of different F thickness, the F spin resistance $R_F = \rho_F \lambda_F / A_I$ should be unaffected to a first approximation due to the empirical relationship discussed in Section B below [S1,S2,S5], *i.e.*, constant $\rho_F \lambda_F$ in a given material.

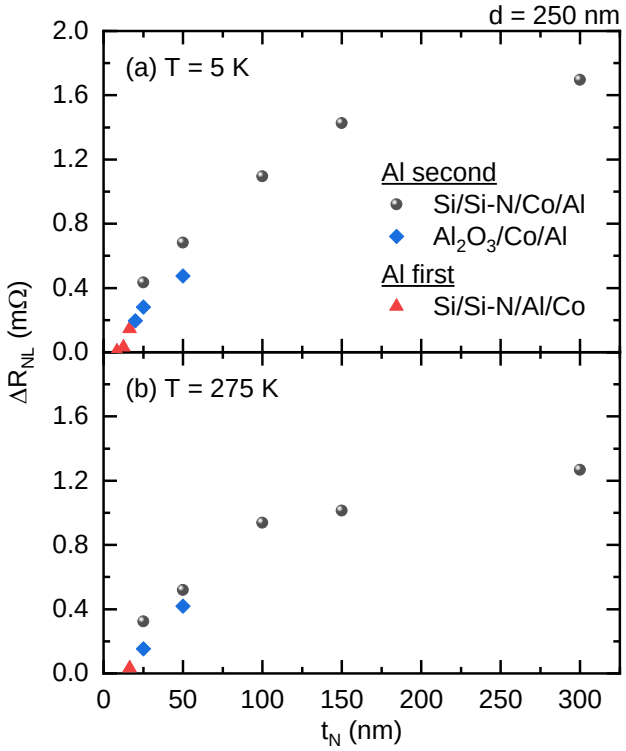

Fig. S1. Spin accumulation signal ΔR_{NL} *vs.* N (Al) thickness t_N for NLSVs with injector/detector separation d = 250 nm, deposited "Al-first, Co-second" (red triangles) and "Al-second, Co-first" (blue diamonds, grey circles). Data are shown at both low (5 K, (a)) and high (275 K, (b)) temperature, not only for the devices on Si/Si-N substrates studied throughout this work but also for additional devices on Al_2O_3 substrates.

Non-local measurements were conducted in AC mode at 13 Hz, using 316 μA excitation, in a continuous flow He cryostat equipped with a superconducting magnet. For all devices, we verified at T = 5 K that this current did not induce significant self-heating, as would be detected by an increase in the non-local background voltage at high current values [S3]. Local measurements to extract resistivity were conducted in a similar manner, with the exception that a smaller bias current of 10-100 μA was sufficient for all thicknesses.

Section B: Fitting Procedure to Extract λ_N

While a transparent F/N interface is expected when employing a single-shot UHV deposition method [S1,S2], this assumption was explicitly verified. Precise resistance-area product determination for metallic interfaces is challenging, but we estimate this here by measuring the resistance $R_{I,M}$ across the F/N interfaces and subtracting a simulated current spreading (or current crowding) contribution $R_{I,S}$ [S1,S2], *i.e.*, using $R_I = R_{I,M} - R_{I,S}$. Simulations were carried out with the commercial COMSOL package. The measurement geometry is illustrated in Fig. S2(a), in which the current and voltage leads are arranged along the arms of a 4-terminal F/N cross such that a current passes through the F/N interface, and the voltage leads are connected to the opposing arms. To account for nonideal asymmetries in the shape of the F/N interface or channels, the experimentally measured $R_{I,M}$ was taken as the average resistance between the wiring configuration in Fig. S2(a), and a wiring configuration in which I- and V- terminals were swapped.

Illustrative simulation results are shown in Fig. S2(a) for a t_N = 50 nm Co/Al NLSV, in which the simulated current spreading voltage $V_{I,S}$ = -71 μV (for I = 316 μA) for a transparent (zero resistance) interface. As noted in our prior work, $V_{I,S}$ is expected to be negative [S1,S2], and so the measured voltage $V_{I,M}$ will also be negative for $R_I < |R_{I,S}|$. Thus, any positive offset with respect to $R_{I,S}$ in the measured $R_{I,M}$ can be attributed to non-zero F/N interface resistance. Measurements of $|R_{I,M}|$ were made across a wide t_N range (8.5–200 nm), as shown in Fig. S2(b). As t_N is reduced, $|R_{I,M}|$ increases significantly, reaching ~1-2 Ω at $t_N \approx$ 10 nm. As shown in Fig. S2(c), however, after accounting for $R_{I,S}$ (from simulations at the same t_N), the resulting interfacial resistance-area product R_IA remains in only the few fΩ m^2 range, consistent with our prior work, and safely satisfying the transparent interface criterion discussed below [S4].

The Takahashi-Maekawa result [S4] for ΔR_{NL} in the transparent interface limit is:

$$\Delta R_{NL} = \frac{4\,\alpha^2 \frac{{R_F}^2}{(1-\alpha^2)^2\,R_N}\, e^{-d/\lambda_N}}{\left(1 + 2\,\frac{R_F}{(1-\alpha^2)\,R_N}\right)^2 - e^{-2d/\lambda_N}}, \tag{S1}$$

where $R_F = \rho_F\lambda_F/A_I$ and $R_N = \rho_N\lambda_N/A_N$ are the spin resistances in the F and N, and the other symbols are defined in the main text. A_I and A_N here are the F/N interfacial area and the cross-sectional area of the channel (determined by the relevant widths and thicknesses), and ρ_F and λ_F

are the resistivity and spin diffusion length of the F. All dimensions were explicitly measured by SEM for each measured device and a correction was made to the measured ΔR_{NL} by scaling it according to Eqn. S1, *i.e.*, by the factor $w_{N,actual}/w_{N,average}$; this accounts for small (~10%) variations in N widths within device sets with varying d [S1,S2]. To determine appropriate values for ρ_F, T-dependent measurements were made on Co nanowires with identical dimensions to those used in NLSVs, yielding (between 5 and 290 K), ρ_F = 21.4–27.5 μΩ cm for t_F = 16 nm, and ρ_F = 10.3–17.2 μΩ cm for t_F = 32 nm. To properly constrain the fitting, λ_F was assumed to follow the established empirical relationship $\rho_F\lambda_F$ = 0.67 fΩ μm^2 [S1,S2,S5]. At T = 5 K, for example, this results in λ_F = 3.1 nm for t_F = 16 nm, and λ_F = 6.5 nm for t_F = 32 nm.

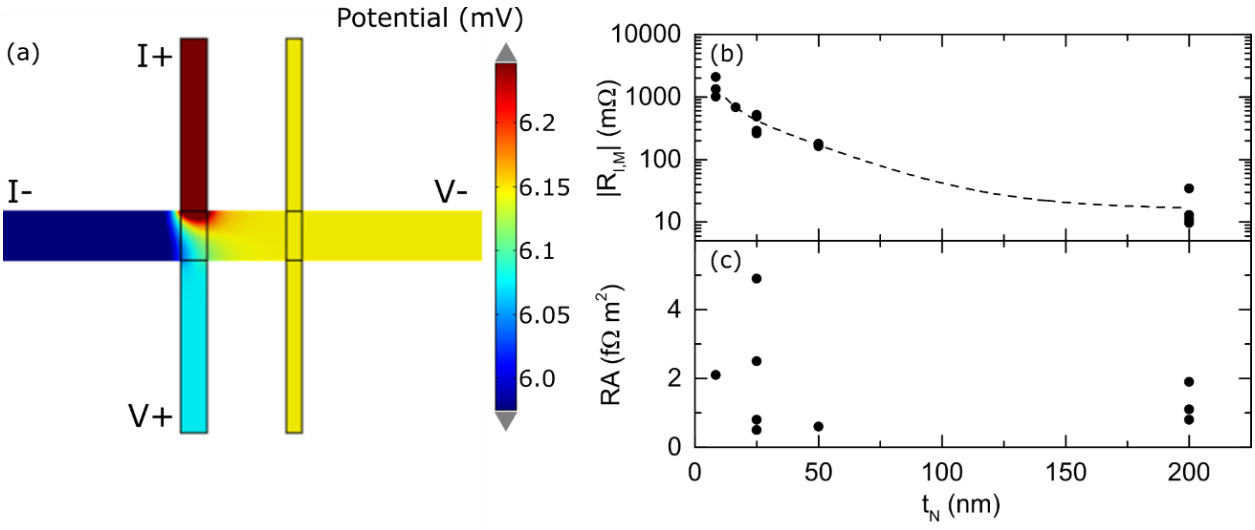

Fig. S2. (a) Interfacial in-plane cross-section of the simulated potential during measurement of the interface resistance $R_{I,M}$ of a Co/Al NLSV with t_N = 50 nm and a transparent (zero resistance) interface. The horizontal bar is the Al channel, and the two vertical contacts are the Co contacts. The scale shown for the potential has been truncated to emphasize the effect of current spreading near the interface. Note that the simulated voltage $V_{I,S}$ is negative [S1,S2]. (b) Absolute value of measured $R_{I,M} = V_{I,M}/I$ for t_N = 8.5–200 nm for both Co/Al and Co/Cu NLSVs. The dashed line is simply a guide to the eye. (c) Deduced interface resistance-area product (R_IA).

$\Delta R_{NL}(d)$ data at various T, as in Fig. 2(a,b), can then be fit to Eqn. S1 with only $\lambda_N(T)$ and $\alpha(T)$ as free parameters. As mentioned in the main text, these parameters are essentially independent,

however, as Eqn. S1 reduces to $\Delta R_{NL} \propto e^{-d/\lambda_N}$ in the high d limit. Simple exponential fits at high d thus determine λ_N, a subsequent fit at all d then yielding α.

Section C: Extracted Spin Transport Parameters

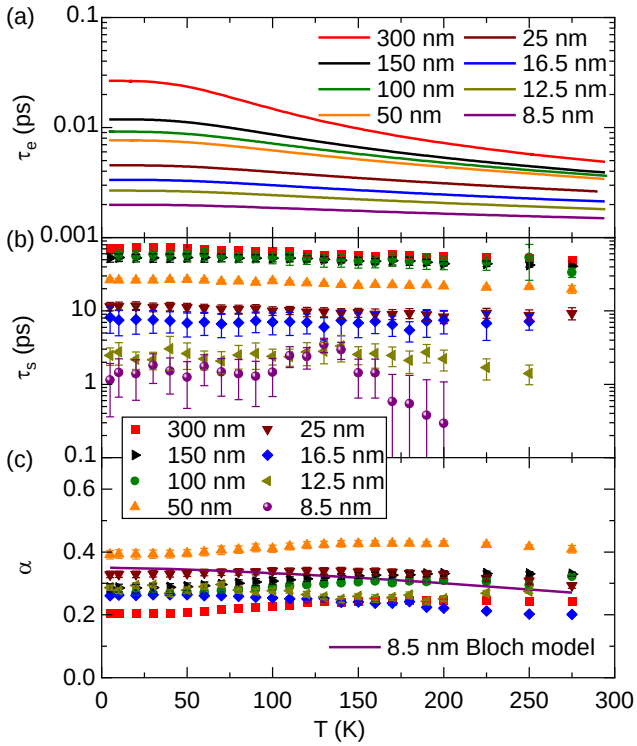

Fig. S3. T dependence of (a) τ_e, (b) τ_s, and (c) α, for Co/Al NLSVs with varied t_N. See Section F regarding the t_N = 8.5 nm case in (c), *i.e.*, the solid line.

The procedure described in Section B results in the t_N-dependent $\lambda_N(T)$ data shown in Fig. 2(c). This was then analyzed in conjunction with the t_N-dependent $\rho_N(T)$ data shown in Fig. 1(c). As discussed in the main text, $\tau_e(T)$ was extracted from $\rho_N(T)$ using $\tau_e(T) = 3D(T)/v_F^2$ (where $v_F = 2.03 \times 10^6$ ms^{-1} is the Al Fermi velocity), and $D(T) = [N(E_F)e^2\rho_N(T)]^{-1}$ (where $N(E_F) = 2.4 \times 10^{28}$ eV^{-1}m^{-3} is the Al density-of-states at the Fermi level and e is the electronic charge) [S6]. $\lambda_N(T)$ was then converted to $\tau_s(T) = \lambda_N^2(T)/D(T)$, generating the $\tau_e(T)$ and $\tau_s(T)$ shown in Fig. S3(a,b) above, for all probed t_N. The comparison of these quantities to determine EY proportionality constants is discussed in detail in the main text. For completeness, also shown in Fig. S3(c) is $\alpha(T)$ for the

same devices. We find $\alpha \approx 0.30$ in all cases (with no systematic t_N dependence), and weak T-dependence, in line with expectations from prior work using Co [S1,S2].

Complementing Fig. 3 in the main text, in Fig. S4 below we also replot the data of Fig. 3(b) such that variations in $\tau_{e,ph}^{-1}$ are more visible. As can be seen, $\tau_{e,ph}^{-1}$ is indeed essentially independent of t_N.

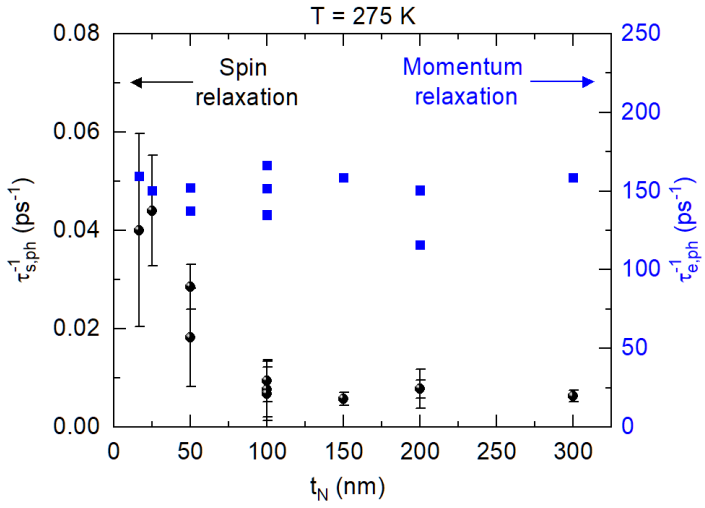

Fig. S4. 275-K t_N dependence of $\tau_{s,ph}^{-1}$ (black, left axis) and $\tau_{e,ph}^{-1}$ (blue, right axis). This is Fig. 3(b) replotted such that any t_N dependence of $\tau_{e,ph}^{-1}$ becomes visible. The t_N dependence of $\tau_{e,ph}^{-1}$ is negligible, however, as discussed in the main text.

Section D: Bloch-Grüneisen Analysis

As discussed in the main text, $\rho_N(T)$ data on Al films and NLSVs were fitted to the Bloch-Grüneisen model [S7,S8] to extract θ_D. This employed

$$\rho_N(T) = \rho_0 + K\left(\frac{T}{\theta_D}\right)^5 \int_0^{\theta_D/T} \frac{x^5 dx}{(e^x - 1)(1 - e^{-x})}, \quad \text{(S2)}$$

where ρ_0 is the residual resistivity and the fitting parameters are the pre-factor K and Debye temperature θ_D. Fit results for the Al NLSVs are shown in Fig. S5(a) below for $\rho_N(T)$ at each thickness, in which experimental data are shown as open circles, and the fits to Eqn. S2 are overlaid as solid lines. For comparison, Fig. S5(b) shows only the phonon contribution to resistivity (in which the residual resistivity ρ_0 has been subtracted from $\rho_N(T)$) for the 300, 25, and 8.5 nm

devices. K was found to be constant at ~15 μΩ cm over a wide t_N range, and the resulting $\theta_D(t_N)$ is shown in Fig. 3(d).

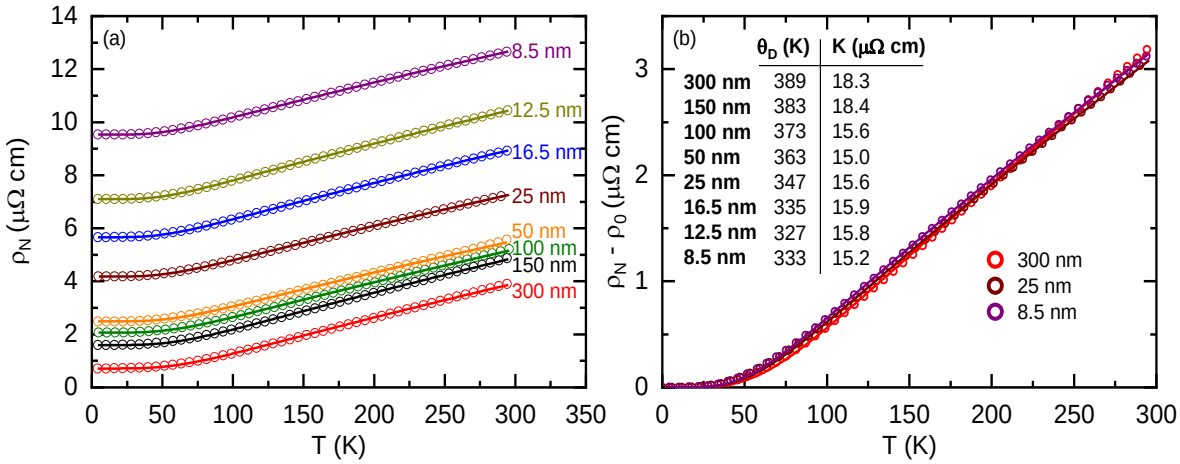

Fig. S5. Example T dependences of the Al resistivity in NLSVs with channel thickness t_N = 8.5–300 nm. Open circles are experimental data (interpolated to identical temperatures for clarity) and solid lines are fits to the Bloch-Grüneisen model described below. Data are shown for the total resistivity ρ_N (a), and for the phonon contribution (b) in which the residual resistivity ρ_0 has been subtracted for the t_N = 300, 25, and 8.5 nm cases. The resulting fit parameters, the Debye temperature θ_D and pre-factor K, are listed in (b) for each thickness.

Section E: Simulation Details

As discussed in the main text, 3D Monte Carlo simulations were employed to quantitatively model enhanced spin relaxation at surfaces/interfaces. As in our prior work where this modeling was developed [S2], we solve the steady-state spin-diffusion equation:

$$\frac{\partial \vec{p}}{\partial t} = D\nabla^2\vec{p} - \frac{\vec{p}}{\tau_s} + \vec{G}(\vec{r}) = 0 \qquad \text{(S3)}$$

in a 3D model using an iterative forward-Euler approach. Here, $\vec{p}$ is the spin polarization in a given discretized cell, t is time, D is the electron diffusivity, τ_s is the spin lifetime, and the spin polarization source term $\vec{G}(\vec{r})$ is non-zero only in the cells just above the injector F (see Fig. 4(a)). The terms in this expression thus represent spin diffusion, relaxation, and injection, respectively. The model geometry is shown in full in Fig. 4(a), and discussed in the main text. The Al channel

of width w_N = 160 nm is decimated into cells where a thickness-adjusted λ_N is used to optimize the cell size: $(\lambda_N/3) \times 40 \times 0.5$ nm^3. The total channel length L is set to $10\lambda_N$, while t_N and the surface/interface thickness t_s are varied. The spin relaxation rate is then specified in each cell:

$$\tau_s^{-1} = \tau_{s,def}^{-1} + \tau_{s,ph,i}^{-1}, \tag{S4}$$

where $\tau_{s,def}^{-1}$ is taken from experiment, and $\tau_{s,ph,i}^{-1} = \beta_{ph,i}^{-1}\tau_{e,ph}^{-1}$ is assigned using either $\beta_{ph,bulk}$ = 26000 in the Al interior (grey cells in Fig. 4) or a specified $\beta_{ph,surf}$ for top and bottom surface cells (blue cells in Fig. 4). $\tau_{e,ph}^{-1}$ is set to the average experimental value for all t_N (Fig. S4): 160 ps^{-1}. The model is then iterated forward in time to find the steady-state spatial distribution $\vec{p}(x)$, enabling extraction of the effective spin lifetime $\tau_{s,eff}$ *via* $\vec{p}(x) = p_0 e^{-x/\sqrt{D\tau_{s,eff}}}$, where the D is extracted from the experimental ρ_N. Finally, the extracted $\tau_{s,eff}$ and experimental $\tau_{s,def}^{-1}$ determine the effective phonon spin relaxation rate $\tau_{s,ph,eff}^{-1} = \tau_{s,eff}^{-1} - \tau_{s,def}^{-1}$, and thus the effective EY phonon parameter $\beta_{ph,eff} = \tau_{e,ph}^{-1}/\tau_{s,ph,eff}^{-1}$. Example raw simulation data are shown in Fig. S6 below, for the conditions given in the legend.

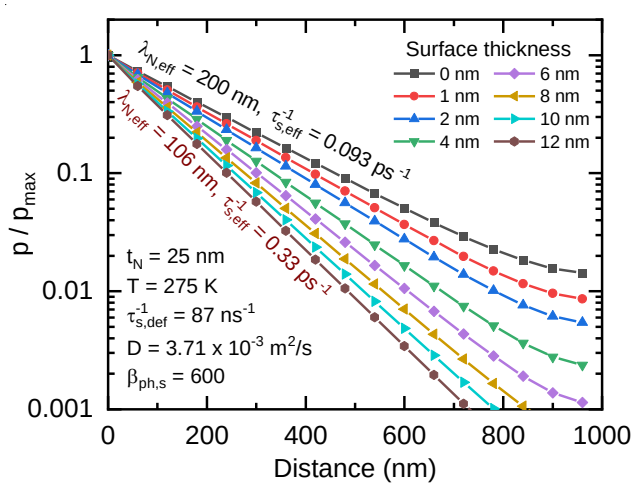

Fig. S6. Normalized spin polarization (p/p_{max}, $\log_{10}$ scale) as a function of N channel distance from the injection cell (see Fig. 4(a)). Simulated results are shown for t_N = 25 nm and T = 275 K, for a range of surface/interface thicknesses (t_s), for $\beta_{ph,s}$ = 600. The resulting effective spin diffusion length $\lambda_{N,eff}$ and corresponding effective spin relaxation rate $\tau_{s,eff}^{-1}$ are shown for the 0 and 12 nm cases. Parameters relevant to the model at the specified thickness and temperature are provided in the legend.

Section F: Additional Low t_N (<10 nm) Analysis

The central result of this work, as shown in Fig. 3(b,c) based on analysis of Fig. 3(a), in no way relies on sub-10-nm-t_N data. As noted in the caption to Fig. 3, t_N = 8.5 nm data are in fact not included in Fig. 3(a) due to various difficulties encountered in this regime. As shown in Fig. 1(d), for example, at t_N = 8.5 nm, ΔR_{NL} falls to the noise floor at high T, even at relatively low d of 250 nm. The ΔR_{NL} data at t_N < 10 nm thus exist over a limited range of d (we do not fabricate devices below d = 150 nm) and T. Compounding this, in this limit, the residual resistivity ratio falls to as little as 1.3 (*cf*. 4.7 at t_N = 300 nm and 15 in unpatterned films), resulting in a very weak T dependence to λ_N and τ_s. All of these factors render extraction of β_{ph} difficult. This is highlighted in Fig. S7(a) below, where τ_s^{-1} at t_N = 8.5 nm is plotted *vs.* $\tau_{e,ph}^{-1}$ (analogous to Fig. 3(a)), along with red and green lines illustrating β_{ph} = 26,000 and 1,000, *i.e*., the full span of what is found in this work. Due to the noise introduced by the small, noisy ΔR_{NL}, the limited d range to determine λ_N and τ_s, the associated limited T range, and the low residual resistivity ratio (and thus small variation in $\tau_{e,ph}^{-1}$), β_{ph} cannot be determined with any accuracy in this set of devices. Data at t_N = 8.5 nm are thus not shown in Fig. 3(a).

Data at t_N = 8.5 nm do appear in Fig. 3(b,c), however (as well as Fig. 4(c)). Those data points were extracted by an alternative procedure that we now describe. The essential idea is to fit the raw $\Delta R_{NL}(T)$ data, or equivalently $\Delta R_{NL}(\tau_{e,ph}^{-1})$, as opposed to $\tau_s^{-1}(\tau_{e,ph}^{-1})$. As shown in Fig. S7(b), such data are relatively noise-free at $d \leq 225$ nm. Based on the fact that the generalized EY concept in the form of Eqn. 1 in the main text is demonstrably valid (from higher t_N data), we substitute $\lambda_N = \sqrt{D/\left(\beta_{ph}^{-1}\,\tau_{e,ph}^{-1} + \beta_{def}^{-1}\,\tau_{e,def}^{-1}\right)}$ (see Eqn. 1 in the main text) in Eqn. S1, enabling fitting of $\Delta R_{NL}(\tau_{e,ph}^{-1})$. To do this reliably we constrain $\alpha(T)$ to a simple Bloch-like $\alpha(T) = \alpha_0\left(1 - AT^{3/2}\right)$, where α_0 and A are constants. α_0 was determined from $\Delta R_{NL}(d)$ at 5 K, while A was fixed based on fits to the higher-T $\alpha(T)$ at higher t_N, resulting in $A \approx 5 \times 10^{-5}$ K$^{-3/2}$ [S6]. The t_N = 8.5 nm solid curve for $\alpha(T)$ in Fig. S3(c) results from this procedure. Final resulting fits to $\Delta R_{NL}(\tau_{e,ph}^{-1})$ are shown in Fig. S7(b), along with the thus-extracted β_{ph} in Fig. S7(c). The four data points are quite consistent, yielding an average β_{ph} of 4480, as plotted in Fig. 3(c), and, more visibly in Fig. 4(c). While admittedly more complex, this procedure in the challenging t_N = 8.5 nm case does indeed

result in β_{ph} values in reasonable agreement with the remaining $\beta_{ph}(t_N)$ data points in Figs. 3(c), 4(c).

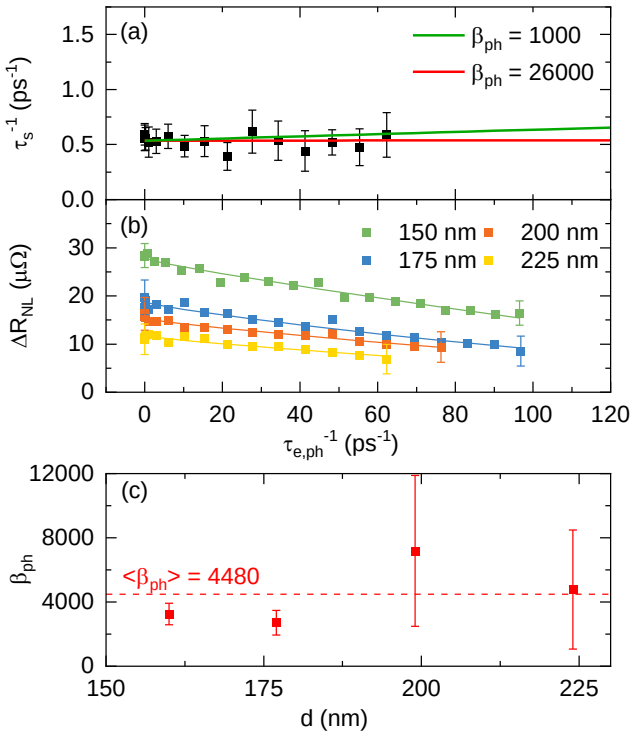

Fig. S7. $\tau_{e,ph}^{-1}$ dependence of (a) τ_s^{-1} and (b) ΔR_{NL} (at multiple d), for t_N = 8.5 nm. The solid lines are fits to the models described above. (c) β_{ph} values extracted from the fits in (b). The average, 4480, is shown as a red dotted line.

References

S1. L. O'Brien, M.J. Erickson, D. Spivak, H. Ambaye, R.J. Goyette, V. Lauter, P.A. Crowell and C. Leighton, *Kondo physics in non-local metallic spin transport devices*, Nat. Commun. **5**, 3927 (2014).

S2. L. O'Brien, D. Spivak, N. Krueger, T.A. Peterson, M.J. Erickson, B. Bolon, C.C. Geppert, C. Leighton, and P.A. Crowell, *Observation and modelling of ferromagnetic contact-induced spin relaxation in Hanle spin precession measurements*, Phys. Rev. B **94**, 094431 (2016).

S3. F. L. Bakker, A. Slachter, J.-P. P. Adam, and B. J. Van Wees, *Interplay of Peltier and Seebeck Effects in Nanoscale Nonlocal Spin Valves*, Phys. Rev. Lett. **105**, 136601 (2010).

S4. S. Takahashi and S. Maekawa, *Spin injection and detection in magnetic nanostructures*, Phys. Rev. B **67**, 052409 (2003).

S5. J. Bass and W.P. Pratt, *Spin-diffusion lengths in metals and alloys, and spin-flipping at metal/metal interfaces: an experimentalist's critical review*, J. Phys. Condens. Matter **19**, 183201 (2007).

S6. N.W. Ashcroft and N.D. Mermin, *Solid State Physics* (Brooks/Cole, New York, 1976).

S7. J. Bass, W. P. Pratt, and P. A. Schroeder, *The Temperature-Dependent Electrical Resistivities of the Alkali Metals*, Rev. Mod. Phys. **62**, 645 (1990).

S8. A. Bid, A. Bora, and A. K. Raychaudhuri, *Temperature Dependence of the Resistance of Metallic Nanowires of Diameter ≥ 15 nm: Applicability of Bloch-Grüneisen Theorem*, Phys. Rev. B **74**, 035426 (2006).